coatings

MDPI

Article

Contrast Role of Third Body Layer and Hard Abrasives in the Wear Process of a TiAlSiN Hardness-Modulated Multilayer Coating: A Case Study on the Effect of Normal Load and Velocity

Fan Zhao *, Zhou Zhu, Jiaxin Yu, Zhiquan Luo and Huimin Qi

Key Laboratory of Testing Technology for Manufacturing Process in Ministry of Education, Southwest University of Science and Technology, Mianyang 621000, China; joshua091@163.com (Z.Z.); yujiaxin@swust.edu.cn (J.Y.); lzq764816062@163.com (Z.L.); huimqi@swust.edu.cn (H.Q.)

* Correspondence: fzhao@swust.edu.cn; Tel.: +86-816-6089708; Fax: +86-816-6089685

Abstract: Working conditions exert an important influence on the tribological properties of protective coatings, thus affecting the wear resistance of workpieces. In this work, a TiAlSiN hardness-modulated multilayer coating with a good match of strength and toughness was deposited on WC-Co substrates. The adhesive wear played a predominant role under the condition of a larger normal load and lower velocity, leading to the formation of a third body layer composed of compressed and lubricating oxides. As a result, the wear rate of the coating tested at 20 N reduced by 23% of that tested at 5 N. Instead, abrasive wear was more manifest, leading to the formation of big-size abrasives, and thus the wear rate increased by 2.8 times while the velocity elevated from 4 mm/s to 16 mm/s. A full factorial analysis of the wear behaviors, including the nanohardness and roughness of the wear track, and the friction coefficient and wear rate of the coating, offered good guidance for the comprehension of the wear form of the TiAlSiN multilayer coating. The results demonstrated the optimization of multilayer structures for TiAlSiN coatings to attain better wear resistance under coupling conditions of normal load and velocity: harder or more lubricated sublayers.

Keywords: TiAlSiN coating; reciprocating friction; wear mechanism; multilayer coating

Citation: Zhao, F.; Zhu, Z.; Yu, J.; Luo, Z.; Qi, H. Contrast Role of Third Body Layer and Hard Abrasives in the Wear Process of a TiAlSiN Hardness-Modulated Multilayer Coating: A Case Study on the Effect of Normal Load and Velocity. *Coatings* **2024**, *14*, 821. https://doi.org/10.3390/coatings14070821

Academic Editor: Frederic Sanchette

Received: 30 May 2024
Revised: 25 June 2024
Accepted: 27 June 2024
Published: 2 July 2024

1. Introduction

Cemented carbides are important components of workpieces in the cutting industry due to their high hardness values and excellent wear resistance [1–3]. However, long-term exploitation of workpieces under harsh environments is often accompanied by the degradation of their performance characteristics. Therefore, the replacement of new pieces occurs very frequently, thus demanding the improvement of properties urgently [4]. Deposition of wear-resistant coatings is an effective solution to improve the surface properties of workpieces instead of fabricating a component wholly from wear-resistant and costly material [5–7]. In particular, the hardness and the frictional properties of coatings, as well as the adhesion between coating and substrate, are very important for the protection of workpieces.

Among the numerous wear-resistant coatings, TiN has been coated on the surface of cemented carbides [8,9]. TiN coating was used for hard coatings in the early 1970s for its considerable hardness, originating from its stabilized face-centered cubic crystal structure where the ratio of the number of atoms of Ti to that of N was about 1:1. However, there is a necessity to update TiN coatings to satisfy the wear resistance of workpieces under more severe working conditions, such as those with no lubrication [10], high velocity [11], large normal load [12], and so on. In particular, the addition of alloying elements [13–15] is an effective approach to improve the application performance of TiN coatings. For instance, the incorporation of Al contributes to the formation of Al_2O_3 oxide layer and draws a barrier between the inner coating and the outside atmosphere, improving the oxidation resistance

of the TiN coating [10,16,17]. Additionally, the addition of Al and Si elements forms a (Ti,Al,Si)N crystal lattice and amorphous silicon nitride, resulting in refined grains [18]. Particularly, TiAlSiN coatings were characterized as being nanocomposites consisting of (Ti,Al,Si)N cubic nano-crystallites embedded in an amorphous matrix of silicon nitride. Therefore, dislocations and other structural defects will become annihilated within the grain boundaries for TiAlSiN coatings, presenting super-hardness values, good wear resistance, and high temperature resistance [17,19,20].

Additionally, these coatings' multilayer structure is also viewed as promising for the optimization of coating performance. Firstly, the interfaces between the sublayers interact with dislocations and act as storage sites for defects, strengthening the multilayer coatings [21,22]. Moreover, multilayers enhance adhesion to substrates by mitigating the interface mismatch, thereby preventing peeling, and improving durability under mechanical and thermal stresses [23,24]. Specially, the gradient multilayers can moderate the variance in thermal expansion coefficients between layers, reducing the stress concentration that leads to delamination, and thus making the coatings tougher [25,26]. Furtherly, the characteristics or thickness conditions of each sublayer lead to different shear stresses and deformations when the coating bears contact load. Currently, the harder sublayer bears more contact load, and the soft one has a lower shear strength [27,28]. Particularly, multilayer coatings with proper cooperation of sublayers have lower residual stress, higher wear resistance, and better adhesion to substrates compared with single-layer coatings [29–31].

Working conditions also exert an important influence on the tribological properties of coatings, affecting the wear resistance of workpieces. For example, the coatings of cutting tools and bearings endure complex working conditions in specific applications such as high-speed cutting and rotating. Therefore, the working atmosphere, contact load, and friction pair all exert an influence on the tribological behaviors of the coating. In the case of high temperatures, the Si element in TiAlSiN coating can react with water in the air to generate SiO_2-H_2O [32], which can reduce the friction coefficient, protecting the coatings from being severely worn. It was also found that the friction coefficient of TiAlSiN coating increased with the increase in normal load [33] and velocity [34] within the bearing range of the coating. In the previous work, we investigated the preparation of TiAlSiN coatings with different hardness values by optimizing the alloy compositions and microstructures [35]. The wear resistance was also improved by regulating the thickness of each sublayer of the TiAlSiN multilayer coatings [36]. However, the wear mechanisms under different conditions need further investigation for the custom design of multilayer coatings to be applied in specific circumstance.

In the present work, TiAlSiN coatings with hardness-modulated sublayers were deposited on the surface of WC-Co substrates by changing the working pressure via the technique of plasma immersion ion implantation and deposition (PIIID). Then, the morphology, cross-sectional element distribution, and mechanical properties of the TiAlSiN hardness-modulated multilayer coatings were investigated. Furthermore, the wear behaviors of the TiAlSiN multilayer coatings under different normal loads and velocities were systematically analyzed. Finally, the relationship between multilayer structures (different combinations of hardness-modulated sublayers) and the wear resistance of the TiAlSiN coatings was discussed in detail.

2. Experimental Details

TiAlSiN multilayer coatings were deposited on WC-Co substrates with PIIID equipment. Prior to deposition, the WC-Co substrates were ultrasonically cleaned with acetone and alcohol for 10 min, sputter-cleaned in pure Aron for 30 min, and then placed in a titanium plasma atmosphere for 30 min. Coating deposition was carried out in a N_2 atmosphere with a TiAlSi (81.76 at. % Ti, 4.01 at. % Al, 14.23 at. % Si) cathode. The composition of TiAlSiN coatings was regulated by the working pressure. Meanwhile, the percentage of sublayers of each modulation period in the alternated multilayer coatings was regulated by the deposition time. Two types of TiAlSiN sublayers with different compositions and har-

ness values were prepared with s working pressure of 0.2 Pa and 0.08 Pa, named sublayer #A and #B, respectively. The ratio of the deposition time of sublayer #A to #B was 2:1 in each modulation period, and the total deposition time was 60 min. The detailed deposition parameters of the TiAlSiN hardness-modulated multilayer coatings are listed in Table 1. The diagram of the equipment and the multilayer structure were shown in Figure 1a,b.

Table 1. Fabrication parameters of TiAlSiN hardness-modulated multilayer coating.

Parameters	Ti Interlayer	#A TiAlSiN Hard Layer	#B TiAlSiN Soft Layer
Target	Ti	$Ti_{81.76}Al_{4.01}Si_{14.23}$	$Ti_{81.76}Al_{4.01}Si_{14.23}$
Working pressure (Pa)	0.008	0.2	0.08
Target current	0.5A (pulse power supply)	50A (direct-current power supply)	50A (direct-current power supply)
Implantation voltage (kV)	15	15	15
Deposition time in each modulation period (min)	/	4	2
Deposition time in total (min)	30	40	20

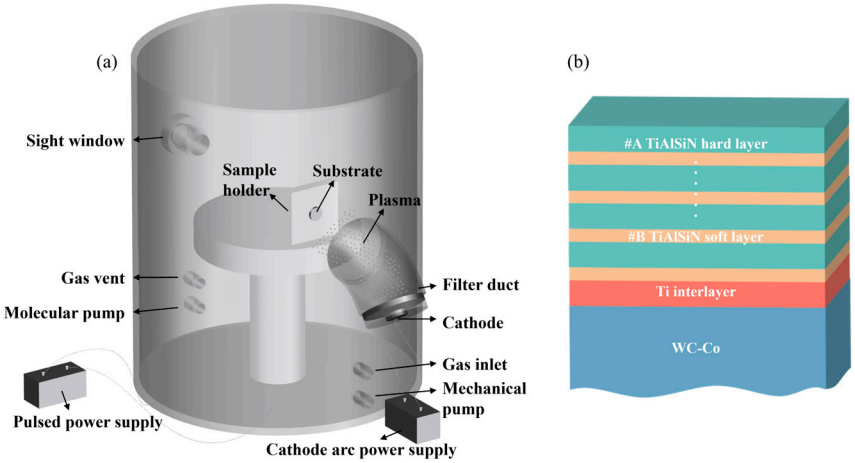

Figure 1. Schematic diagram of TiAlSiN multilayer coating: (**a**) preparation equipment; (**b**) multilayer structure.

The surface morphology of the TiAlSiN multilayer coating was examined using a field-emission scanning electron microscope (FE-SEM, Zeiss Ultra 55, Oberkochen, Germany). The roughness and thickness of the coating were characterized using a white light interferometer (WLI, Rtec-UP2000, San Jose, CA, USA). The cross-sectional morphology and elemental distribution of the multilayer coatings were observed using a transmission electron microscope (TEM, Talos F200X, Waltham, MA, USA). The elemental composition analysis of the coating and wear debris was carried out using an energy-dispersive spectrometer integrated with a field emission scanning electron microscope (EDS, Oxford IE450X-Max80, Abingdon, UK). The nanohardness and Young's modulus of the multilayer coating were measured and determined using a nano indenter (G200, Keysight, Santa Rosa, CA, USA) in continuous stiffness loading mode, where the indentation depth was approximately 1/10 of the thickness of the TiAlSiN multilayer coating to ensure that the test results were not influenced by the hardness of the substrate. The adhesion performance of the TiAlSiN multilayer coating was assessed utilizing a scratch tester (MFT-4000, Lanzhou Huahui Instrument Technology, Lanzhou, China) with a loading rate of 80 N/min, a scratch velocity of 3 mm/min, and a terminal load of 160 N [37].

A multifunctional friction and wear tester (MFT3000, Rtec, San Jose, CA, USA) was used to test the reciprocating friction and wear under atmospheric conditions. To ensure the stability of the wear process and the universality of the tested results, an Al_2O_3 ball with a diameter of 4 mm, commonly used in friction tests, was used as the sliding counter

body. A full factorial experiment with 2 factors and 4 levels was adopted to investigate the influence of normal load and velocity on the wear behavior of the TiAlSiN multilayer coating. The wear test parameters are shown in Table 2, where the contact stresses of the system are 2230, 2810, 3217, and 3540 MPa, corresponding to the normal loads of 5, 10, 15 and 20 N, respectively. There were 16 friction tests in total in our experiment. To ensure the reliability of the test results, each test of the corresponding parameters was repeated three times.

Table 2. Wear test parameters.

Experimental Factors	Values			
Normal load/N	5	10	15	20
Velocity/mm·s^{-1}	4\8\12\16	4\8\12\16	4\8\12\16	4\8\12\16
Displacement amplitude/mm	4	4	4	4
Test time/min	30	30	30	30

The surface morphology of the wear tracks was studied using SEM. The three-dimensional morphology, cross-sectional profile curve, and surface roughness of the wear tracks were characterized using a white light interferometer. Three cross-sectional profiles were determined to calculate the average wear volume and wear rate; from the middle, this was 0.5~1 mm from the two ends. The wear rate of the coating was calculated using the following formula, $W = V/(F \times S)$, where V represents the wear volume, F denotes the normal load, and S signifies the sliding distance. Additionally, the composition of the wear track was investigated and analyzed using an energy-dispersive spectrometer and a Raman spectrometer (inVia, Renishaw, Wotton-under-Edge, UK).

3. Results

3.1. Morphology and Composition of TiAlSiN Multilayer Coating

The surface morphology of the TiAlSiN multilayer coating was observed through field emission scanning electron microscopy, as depicted in Figure 2a. There were some defects, such as large particles, pinholes, and pits distributed randomly on the surface of the coating, which were inevitable during the deposition process [38]. The presence of these large particles was primarily attributed to the metal particles being in a molten state, which were not completely filtered by the magnetic filter bend and splattered onto the coating surface [39]. The formation of the pits could be attributed to the detachment of these large particles, while the presence of pinholes was a consequence of the constriction of the molten particles during the solidification process [39]. However, through all this, the other part without defects showed a dense morphology, which could also be detected via 3D topography, as shown in Figure 2b. Additionally, the surface roughness of the coating could also be measured using the white light interferometer, giving a value of 45 nm. The dense coating could have contributed to the high-energy ion bombardment during the process of PIIID [40]. Moreover, the thickness of the coating was detected due to its 2D profile with a value of 2.4 μm, as shown in Figure 2c. The deposition rate of the coating was about 40 nm/min, which was increased to about four times of the previous one [41], which could be attributed to the adoption of the direct-current power source instead of the pulse power source for the cathode.

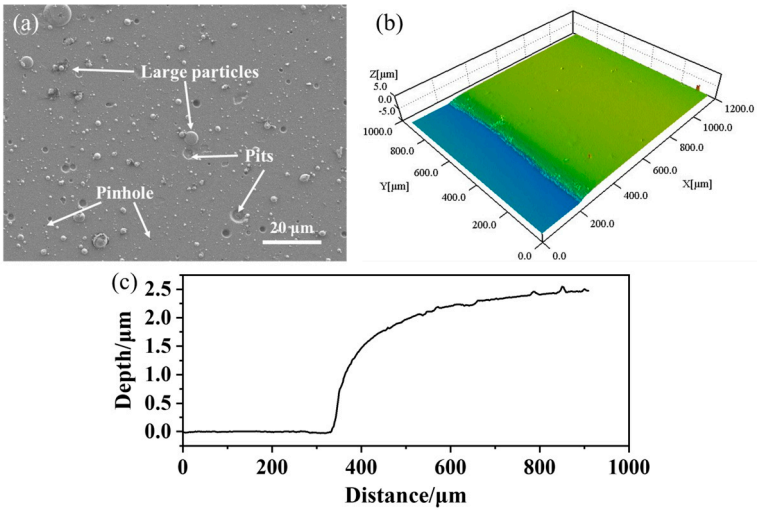

Figure 2. Surface morphology and cross-sectional profile of the coating: (**a**) surface morphology observed via SEM, (**b**) surface morphology determined using the WLI, and (**c**) cross-sectional profile determined using the WLI.

The cross-sectional TEM image of the multilayer coating is shown in Figure 3a, where the grains are oriented and well developed between the alternating soft and hard layers along the growth direction. It could also be observed that the multilayer coating had a dense structure, and the sublayers were integrated closely, almost showing no defects among the interfaces. Additionally, the interfaces between the substrate and Ti interlayer, as well as the hard and the soft sublayers, were irregular and blurry, as shown in Figure 3a. Moreover, the distribution of the elements on the cross-section of the multilayer coating is clearly represented in Figure 3b–f. It is obviously shown that the elements Ti, Al, Si, and N possessed alternate compositions between the hard and the soft sublayers, as shown in Table 3. Particularly, there was a thin layer of Ti originating from ion implantation before the deposition process, as shown in Figure 3c.

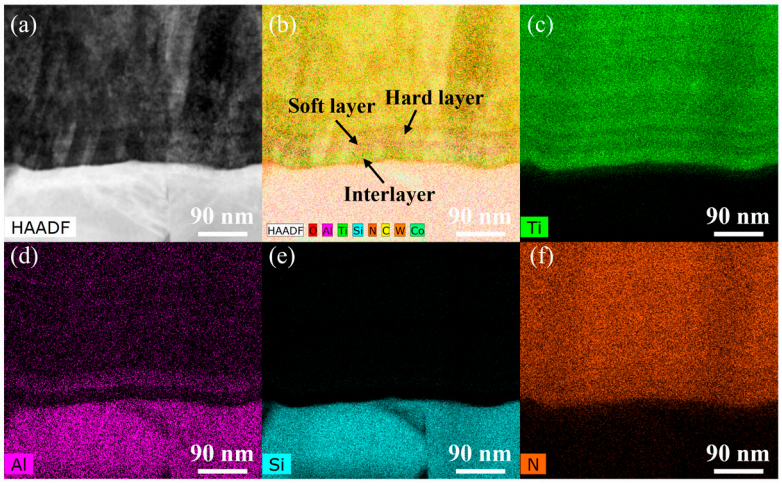

Figure 3. Cross-sectional morphology and element distribution of TiAlSiN multilayer coating: (**a**) cross-section morphology, (**b**) elemental distribution, (**c**) distribution of Ti element, (**d**) distribution of Al element, (**e**) distribution of Si element, and (**f**) distribution of N element.

Table 3. The composition of the TiAlSiN sublayers.

TiAlSiN SUBLAYER	Element Content (at. %)			
	Ti	Al	Si	N
#A	36.08 ± 1.76	1.09 ± 0.05	3.54 ± 0.17	59.30 ± 2.93
#B	44.06 ± 2.18	1.33 ± 0.06	2.56 ± 0.12	52.05 ± 2.59

3.2. Mechanical Properties of TiAlSiN Multilayer Coating

The mechanical properties of the multilayer coating are presented in Table 4. The nanohardness and elastic modulus of the multilayer coating showed average values of 37 GPa and 418 GPa, which were between the values of the two single-layer coatings [36]. Moreover, the calculated H/E^* and $H^3/(E^*)^2$ values of the multilayer coating were about 0.089 and 0.29 GPa, suggesting that the as-deposited TiAlSiN multilayer coating possessed remarkable resistance to both plastic and elastic deformation [12,42]. Additionally, the evaluation was further reinforced by the scratch test, where the coating showed an adhesion strength of 144 N [36].

Table 4. Element content and mechanical properties of coating.

Sample	Nanohardness (GPa)	Elastic Modulus (GPa)	H/E^*	$H^3/(E^*)^2$ (GPa)	Adhesion (N)
TiAlSiN	37.24 ± 0.96	418.52 ± 18.51	0.089	0.29	144

3.3. Tribological Properties of TiAlSiN Multilayer Coating

3.3.1. Effect of the Normal Load on the Wear Behavior of TiAlSiN Coating

A full factorial experiment with two factors and four levels was designed to investigate the influence of normal load and velocity on the tribological properties of the TiAlSiN multilayer coating. Firstly, the friction curves of the as-deposited TiAlSiN multilayer coating under different normal loads at a constant velocity of 4 mm/s are illustrated in Figure 4a. The average frictional coefficient of the coating tested at a load of 5 N, 10 N, 15 N, and 20 N was about 0.46, 0.38, 0.36, and 0.3, respectively. The results showed that a larger normal load led to a smaller frictional coefficient, which is inconsistent with published papers [29]. Three-dimensional morphology and cross-sectional profile curves of the wear tracks are also depicted in Figure 4b,d. The morphology of the worn ball is shown in Figure 4e, where the diameters of the circular planes after the wear tests show values similar to the widths of the wear tracks of the coating. It was evident that there was a slight augmentation in both the width and depth of the wear track, namely the wear volume, as the normal load increased. Furthermore, the debris inside the wear track gradually became more and more compressed with the increase in normal load, resulting in a smoother scratch. Figure 4c shows that the wear rate of the multilayer coating decreased with the increase on the normal load, suggesting an opposite result to the conventional pattern [12,43]. The wear rate of the multilayer coating tested at 20 N reduced by 23% compared with that tested at 5 N.

The wear morphologies of the wear tracks are depicted in Figure 5. The morphology of the wear track tested at 5 N reveals the presence of discernible abrasive particles, which probably augmented the coefficient of friction and exacerbate the wear process, as shown in Figure 5a. Specifically, a small quantity of abrasive chips were distributed inside the wear track tested at 10 N, displaying an adhesion phenomenon within the wear track, as shown in Figure 5b. Furthermore, a few abrasive chips, along with irregular pits and fine grooves, could be observed within the wear track when the normal load was elevated to 15 N, as shown in Figure 5c. Notably, the morphology of the wear track tested at 20 N bore similarity to that tested at 15 N, as shown in Figure 5d. These tracks appeared relatively smooth, exhibiting a few tiny grooves and abrasive chips.

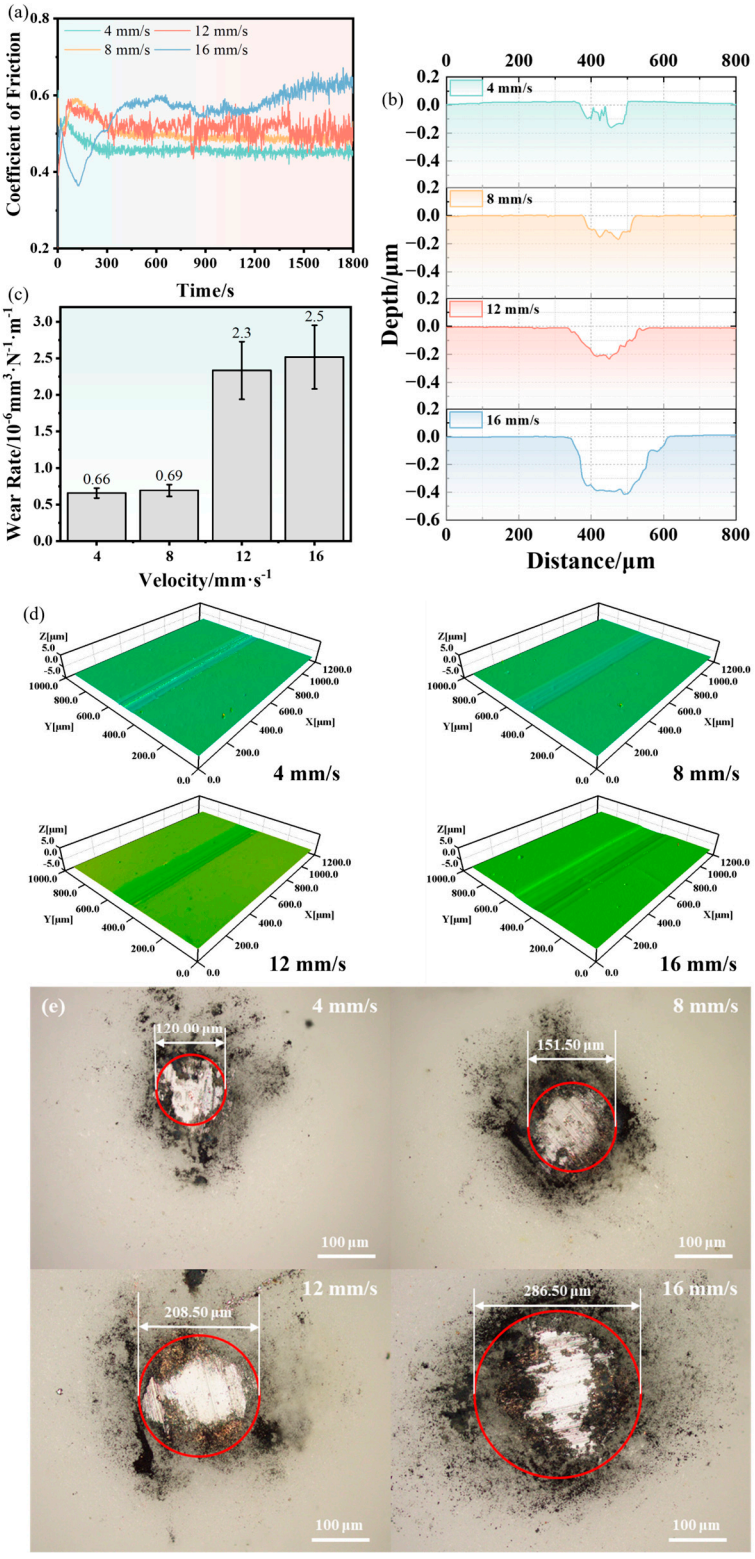

Figure 4. Wear results under different normal loads: (**a**) frictional coefficient, (**b**) cross-sectional profile curve of wear track, (**c**) wear rate, (**d**) 3D morphology of wear track, and (**e**) morphology of sliding ball.

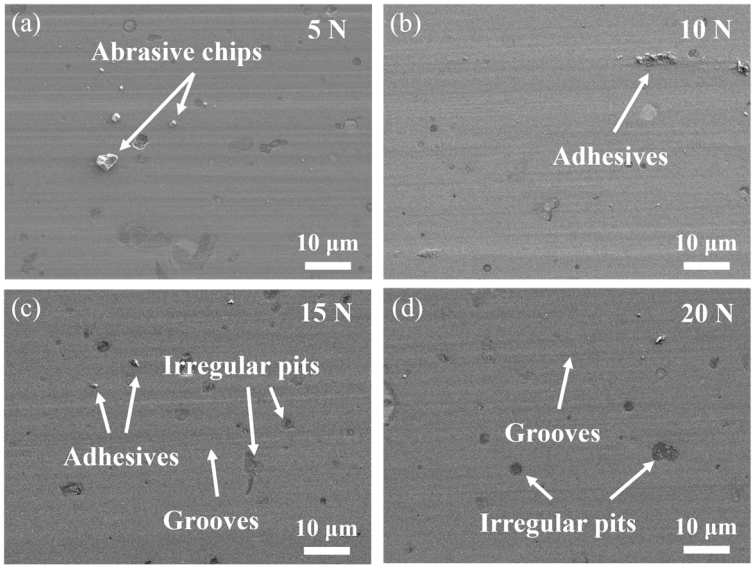

Figure 5. SEM images of wear tracks under different normal loads: (**a**) 5 N, (**b**) 10 N, (**c**) 15 N, and (**d**) 20 N.

To conduct further analysis of the wear debris, the composition of the original coating and the wear track tested at 20 N and 5 mm/s was investigated, as shown in Figure 6. The compositions tested at position 1 and 2 are illustrated in Table 5. The content of Al and O elements inside the wear track increased compared with that in the original coating. The increasing Al and O content could have been due to the abrasive chips from the friction ball that were inevitably retained during the wear process. Notably, the more significant increase in oxygen content may be related to the oxidation of elements, such as Ti, Al, and Si, during the wear process.

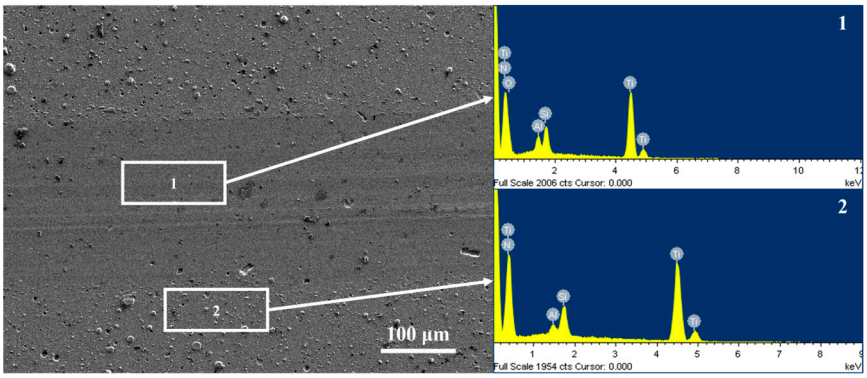

Figure 6. EDS results of the original coating and the wear track.

Table 5. Content of elements inside and outside the wear track.

Sample	Atomic Fraction/%				
	Ti	Al	Si	N	O
1	46.06 ± 2.21	3.29 ± 0.16	6.23 ± 0.32	22.53 ± 1.12	21.89 ± 1.06
2	47.00 ± 2.34	2.02 ± 0.10	5.96 ± 0.29	45.03 ± 2.24	-

Additionally, the Raman spectroscopy of the wear debris tested at different normal loads is exemplified in Figure 7. Particularly, the wear debris primarily comprised as the oxides TiO_2, Al_2O_3, and SiO_2 [14], TiO_2 with peaks of 227 cm^{-1} and 600 cm^{-1} showed the highest intensity [44–46], followed by Al_2O_3 peaks at 323 cm^{-1} and 811 cm^{-1} [14,47], and

a SiO_2 peak at 468 cm^{-1} [32]. Moreover, there was almost no change in the position of these Raman peaks among the wear tracks tested at different normal loads, suggesting that the types of oxides were almost unchanged. However, the intensity of these Raman peaks increased with the normal load, signifying a gradual increasement in the oxide content.

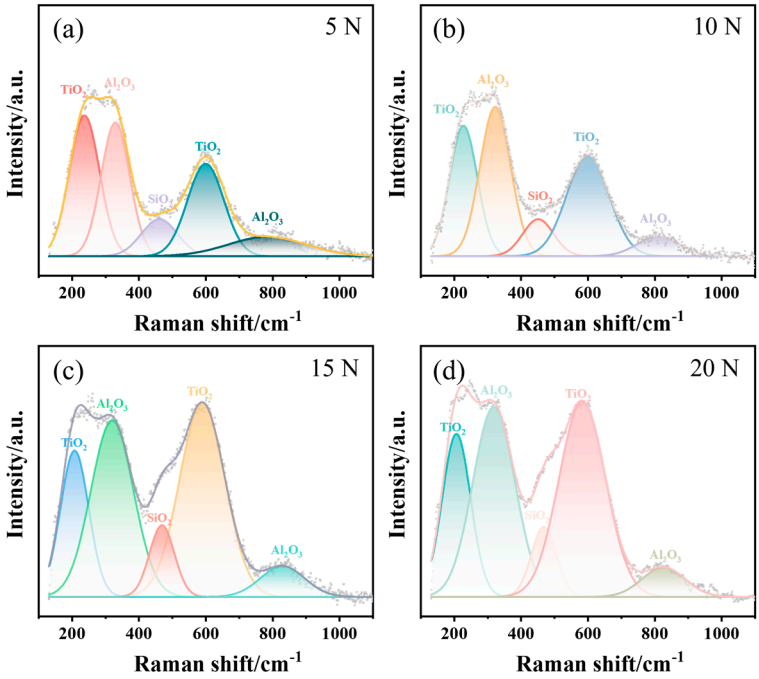

Figure 7. Raman results of wear debris in wear tracks under different normal loads: (**a**) 5 N, (**b**) 10 N, (**c**) 15 N, and (**d**) 20 N.

Remarkably, the nanohardness and roughness of the wear tracks were also examined, as shown in Figure 8. Figure 8a shows the nanohardness inside the wear track tested under different normal loads. Obviously, the nanohardness of all the wear tracks increased compared with that of the original coating. Furthermore, the nanohardness of the wear track increased with the normal load, which further confirmed the compaction of the wear products. Moreover, the roughness of the wear track is delineated in Figure 8b; the larger the normal load, the smaller the surface roughness of the wear tracks. This striking phenomenon could be attributed to the crushing and gradual compaction of the abrasive particles under larger normal loads.

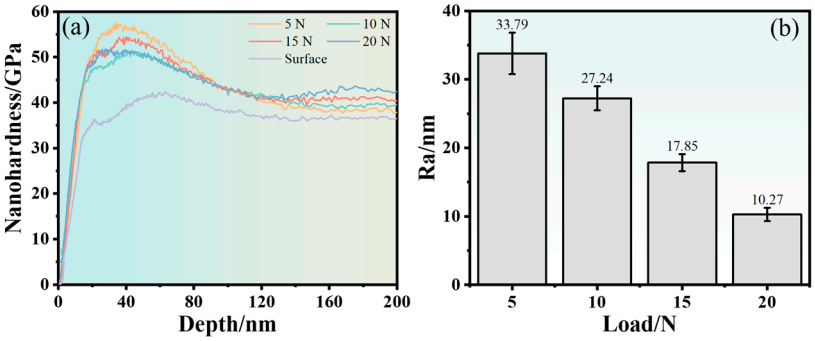

Figure 8. Nanohardness and roughness of the wear tracks under different normal loads: (**a**) nanohardness; (**b**) roughness.

3.3.2. Effect of Velocity on the Wear Behavior of TiAlSiN Coating

Figure 9a presents the friction curves of the coating tested under different velocities, while maintaining a constant normal load of 5 N, with a test time of 30 min. The coating showed an increased friction coefficient value and a magnified fluctuation of the friction curve with the velocity increasing from 4 mm/s to 16 mm/s, accompanied by an increasing reciprocating frequency and total wear length. For example, as the velocity reached 16 mm/s, the friction process appeared to be in a fluctuating state, and stabilized firstly with a frictional coefficient of 0.55. Subsequently, the frictional coefficient increased and stabilized at a value of 0.61 with sustained sliding. Furthermore, the 3D and 2D morphology were characterized to investigate the cross-section profiles of the wear tracks, as illustrated in Figure 9b,d. The morphology of the worn ball is shown in Figure 9e, where the diameters of the circular planes after the wear tests show values similar to the widths of the wear tracks of the coating. Specifically, the width and depth of the wear tracks exhibited a progressive augmentation with increasing velocity. The wear rates of the coating under different velocities were calculated according to the above results, as shown in Figure 9c. It was demonstrated that the wear rate remained almost unchanged with the velocity increasing from 4 mm/s to 8 mm/s, but that it increased significantly from a velocity of 12 mm/s to 16 mm/s. Therefore, it could be concluded that the higher velocity showed a more significant impact on the friction coefficient of the coating.

Additionally, the morphologies of the wear tracks under different velocities are characterized in Figure 10. A small amount of abrasive chips could be detected on the wear track tested at a velocity of 4 mm/s, as shown in Figure 10a. Figure 10b reveals an increasement in the number of irregular pits and abrasive chips within the wear track at a velocity of 8 mm/s. Furthermore, the number of abrasives within the wear track increased more obviously when the velocity was elevated to 12 mm/s and 16 mm/s, compared with that under smaller velocities. Accordingly, a large proportion of abrasives could accelerate the wear of the coating and result in larger wear rates at higher velocities.

The nanohardness and surface roughness of the wear tracks tested at different velocities were also investigated, as depicted in Figure 11. Notably, the nanohardness of the wear tracks showed larger values, compared with those of the original coating, as shown in Figure 11a. The larger nanohardness values may be related to the formation of the hard particles inside the wear track, as well as the crushing of the friction ball. Figure 11b shows the surface roughness of the wear tracks tested at different velocities. It was evident that the roughness of the wear track increased with the velocity, which could have contributed to the increased number of abrasive particles, as shown in Figure 10. In fact, the variation in roughness could serve as a compelling explanation for the more prominent fluctuation of the friction curve at a higher velocity, as illustrated in Figure 9a.

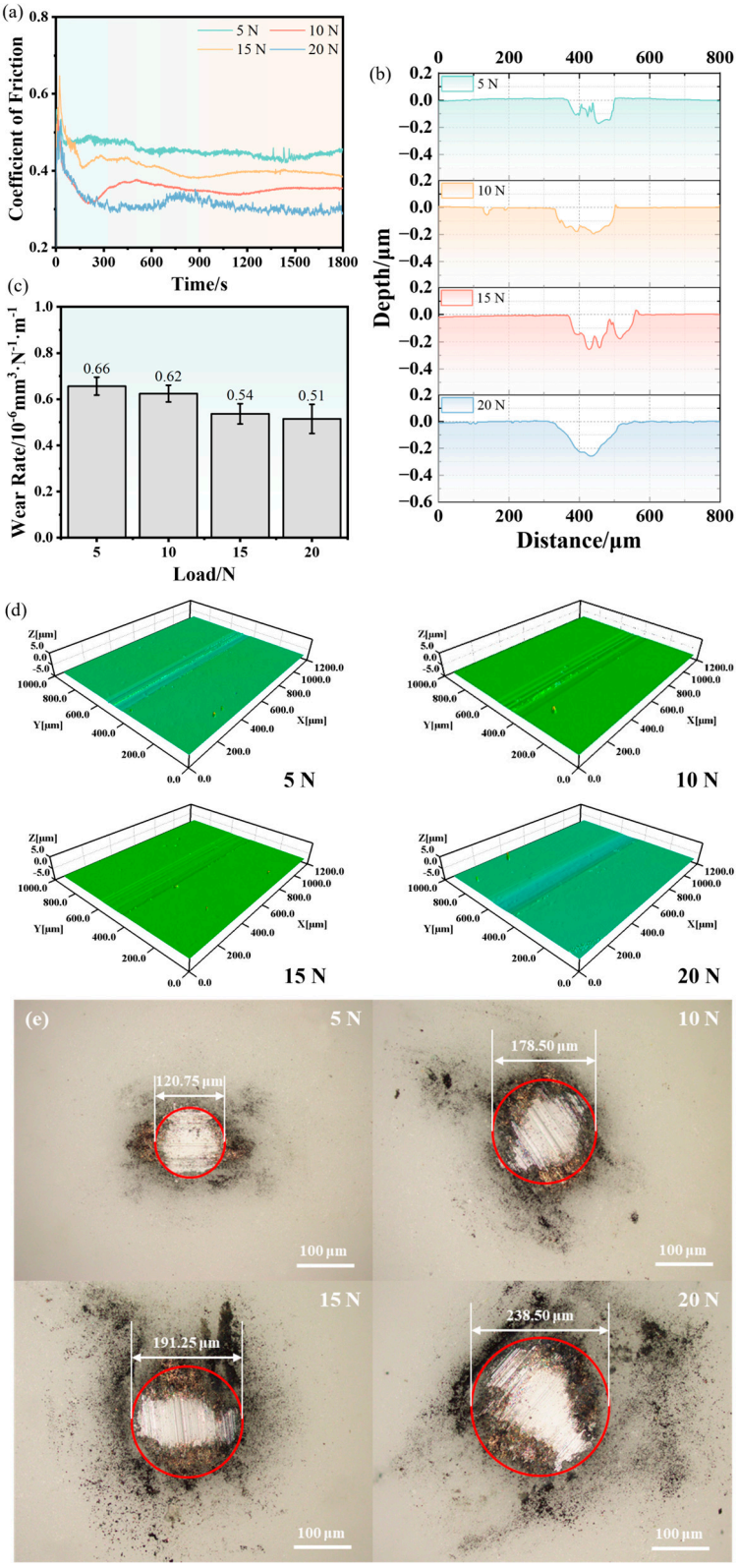

Figure 9. Wear results of coatings at different velocities: (**a**) frictional coefficient, (**b**) cross-sectional profile curves of wear track, (**c**) wear rate, (**d**) 3D morphology of wear track, and (**e**) morphology of sliding ball.

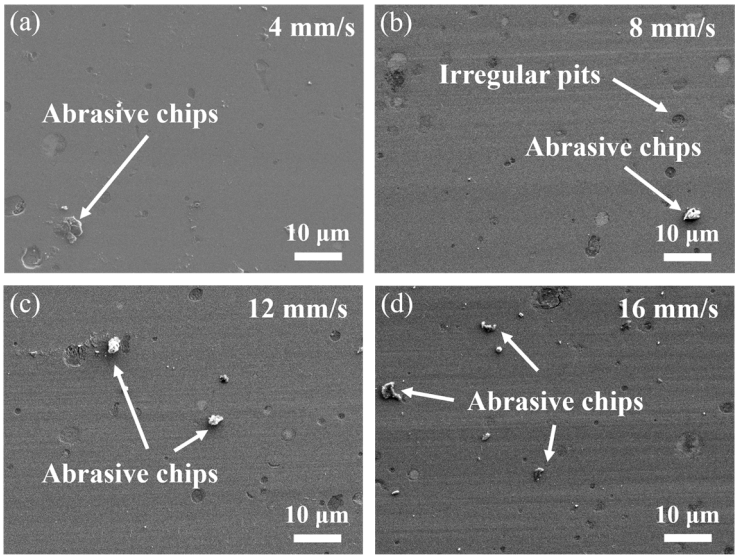

Figure 10. SEM images of wear track under different velocities: (**a**) 4 mm/s, (**b**) 8 mm/s, (**c**) 12 mm/s, and (**d**) 16 mm/s.

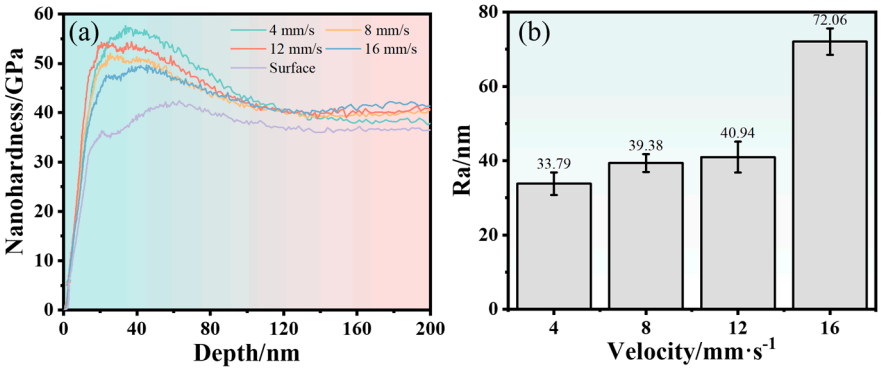

Figure 11. The nanohardness and roughness of the wear track tested at different velocities: (**a**) nanohardness; (**b**) roughness.

3.3.3. The Wear Behavior under the Load–Velocity Coupling Case

The effect of normal load and velocity on the wear behavior of the coating are expressed by the results of factor analysis in accordance with the total tests, as shown in Figure 12. The friction coefficient and wear rate of the coating and the roughness of the wear track decreased, and the nanohardness of the wear track increased with the increasement in the normal load, as shown in Figure 12a. The four parameters showed a similar trend of increasement with velocity, as shown in Figure 12b.

Additionally, the wear results in the load–velocity coupling case were investigated with the response surface methodology, as described in Figure 13. Figure 13a–d present the influence of the load–velocity coupling case on the nanohardness and roughness of the wear track, as well as the friction coefficient and wear rate of the coating. According to the slope in the surface diagram shown in Figure 13a, the nanohardness of the wear track reached a higher value under the conditions of higher load and velocity, and vice versa. Similarly, larger roughness of the wear track was observed under the conditions of smaller normal load and higher velocity, as shown in Figure 13b. Moreover, the friction coefficient and wear rate of the coating reached a higher value under the conditions of smaller normal load and higher velocity, as shown in Figure 13c,d, respectively.

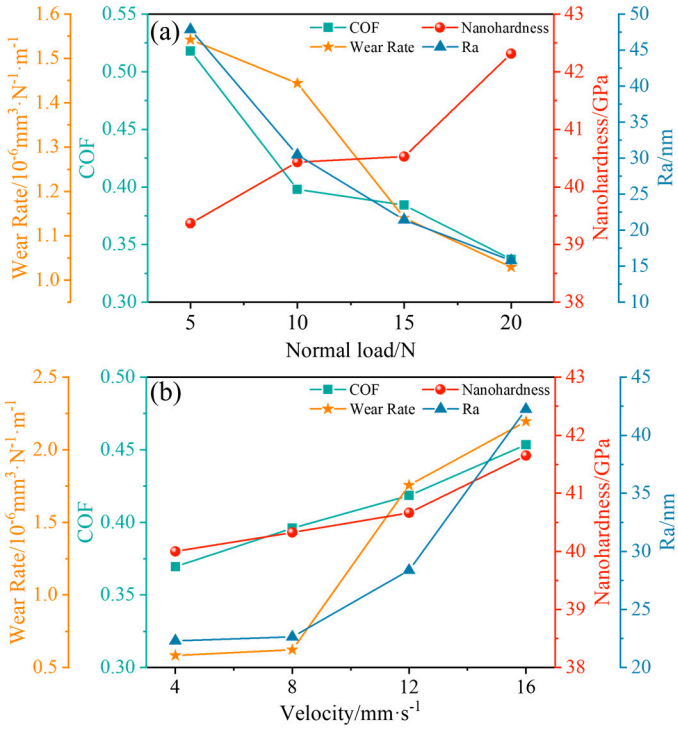

Figure 12. Influence of normal load and velocity on friction results: (**a**) normal load; (**b**) velocity.

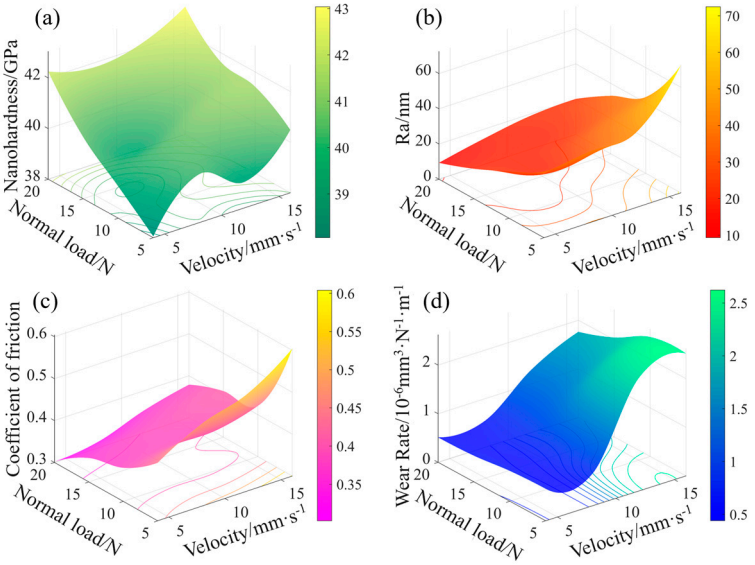

Figure 13. Effect of normal load and speed on tribological properties of coatings: (**a**) nanohardness of wear track, (**b**) roughness, (**c**) friction coefficient, and (**d**) wear rate.

Furthermore, the effectiveness of the normal load and velocity, as shown in the wear results, was observed via analysis of variance, as shown in Table S1 (Supplementary Materials). Particularly, the normal load exerted a greater effect on the nanohardness and roughness of the wear track, with the contribution values of 65.65% and 62.76%. Moreover, the velocity was similarly found to have a minor effect, with a contribution value of 22.44% and 27.75%. Additionally, increasing the normal load led to a more obvious variation in the friction coefficient, with contribution values of 77.63%. By contrast, the velocity was more significant for the wear rate of the coating, with a contribution value of 86.84%. For the measured factors, the p value for the F variable value was less than the probability of error of type I, 0.05, indicating the accuracy of the prediction [48].

4. Discussion

4.1. Enhanced Strength and Toughness of the Coating

Generally, it seems impossible to achieve both strength and toughness for our coating, which has been an enduring pursuit [49]. For example, in our previous study, the harder TiAlSiN single-layer coating showed a nanohardness value of 41.43 GPa, and an adhesion value of 20.8 N while the softer single-layer coating showed a nanohardness value of 33.71 GPa, and an adhesion value of 105.1 N [36]. Moreover, the TiAlSiN coatings deposited via magnetron sputtering showed a larger nanohardness value of 21.79 GPa with a lower adhesion value of 28 N, or possessed a smaller nanohardness of 15.25 GPa with a higher adhesion value of 95.7 N [50]. In fact, the as-deposited multilayer coating was not only strengthened but also toughened, possessing a nanohardness value of 37 GPa and an adhesion value of 144 N.

Moreover, the enhancement in the strength and toughness of the coating could also be detected via the morphologies of the wear tracks shown in Figures 5 and 10, showing almost no cracks, peeling, or delamination. The excellent mechanical properties of the coating could be attributed to the proper stress distribution inside the hard and soft alternated sublayers, as well as the dense structure and the highly reinforced interfaces of the coating. It should be noted that this study has examined the dense structure and highly bonded interfaces between the substrate and the Ti interlayer, as well as the harder and softer sublayers. The stress distribution inside the sublayers of the coating could be investigated in future. We have to point out that the irregular and blurry interfaces (as shown in Figure 3) originated from the ion bombardment during the implantation operation [41], promoting the bonding and mechanical properties of the coating to a large extent [21,51]. In fact, the bonded interface could be considered one of the most important factors affecting the application of wear-resistant coatings.

4.2. Third Body Layer and Hard Abrasive Wear Mechanisms

Furthermore, the multilayer coating possessed different wear behaviors while the normal loads and velocities varied. As the normal load increased, the wear debris including the lubricant oxides within the wear track underwent gradual pulverization and compaction, ultimately resulting in a smoother surface inside the wear track. To a certain extent, the smoother surface contributed to a smaller friction coefficient and stable friction process, as can be seen in Figure 4a. The smoother surface could also be detected via the morphologies and roughness of the wear track, shown in Figures 5 and 8b, separately. Additionally, the nanohardness of the wear track increased with the normal load because of the reciprocating rolling and the grinding pair [52]. As a result, the wear track tested under larger normal loads possessed a smoother surface, this being derived from the compaction of the wear debris during the wear process. Consequently, the oxide debris compressed during the wear process could form a lubricating third body layer [53,54], thus resulting in a smaller friction coefficient and reduced wear rate. In contrast, the wear debris evolved toward becoming big-size abrasives, resulting in an increased roughness of the wear track and the increased friction coefficient of the coating. Worse still, the nanohardness of the wear track also increased to a certain extent with the rising velocities, reciprocating frequency, and total wear length, accelerating the abrasive wear of the coating.

Based on the above analysis of the structure and wear behavior of the TiAlSiN hardness-modulated multilayer coating tested under different wear conditions, two wear models are proposed (Figure 14). Particularly, Model-I usually occurs under the conditions of larger normal load and smaller velocity, as shown in Figure 13a. At the beginning of the wear process, small chips derived from the protrusions on the surface the coating were transferred to the depressions and formed a third body layer under the condition of larger normal loads. The hardened, ground, and lubricated third body layer formed on the surface of the wear track led to larger nanohardness values and smaller friction coefficients, protecting the inner coating from further abrasion and showing a decreased wear rate under larger normal loads. However, the coating tested under the conditions of smaller normal

load and larger velocity was more likely to fall under Model-II, as depicted in Figure 14b. In contrast, the small chips derived from the protrusions on the surface could be transferred quickly, and could not fill in the depression in the coating, thus forming big-size abrasive chips. Although the compaction of the debris was not obvious, the wear track also had larger nanohardness because of the faster, more frequent, and longer reciprocating grinding of the friction pair, as well as the more severe work hardening of the wear track, at a higher velocity. As a result, the wear debris turned from being composed of tiny particles into being made up of big-size and high-hardness abrasives, resulting in an increased friction coefficient and wear rate.

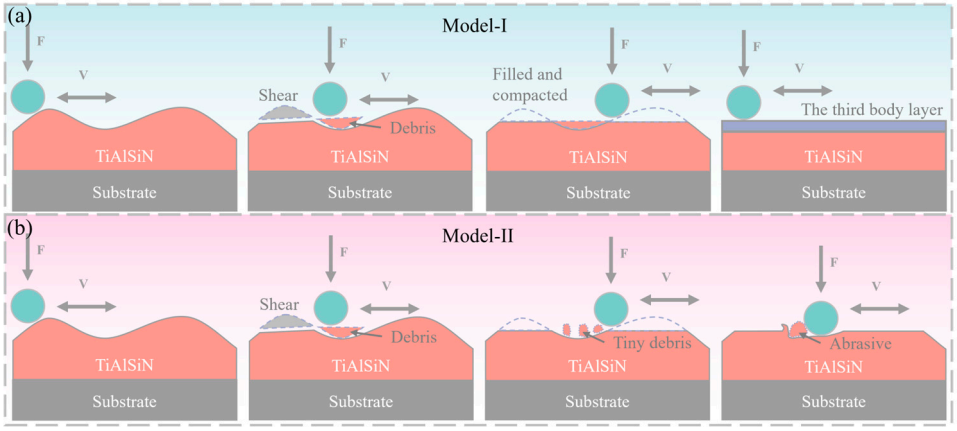

Figure 14. Schematic diagram of wear mechanism: (**a**) the conditions of larger normal load and lower velocity; (**b**) the conditions of smaller normal load and higher velocity.

4.3. New Method to Analyze the Wear Mechanism of the TiAlSiN Coating

As for the coating tested under the conditions of larger normal load and higher velocity, as well as the conditions of smaller normal load and lower velocity, the wear results were more complicated. For example, as the normal load increased, the friction coefficient of the coating became a smaller value because of the compaction of wear debris. However, the increasing velocity could result in more big-size abrasives, resulting in a larger friction coefficient. Although the normal load affected the friction coefficient more than it did the velocity, the impact of the two parameters cannot be quantified. Additionally, the hardening of the wear track protected the coating from being abrased more severely for Model-I, while it accelerated the wear process for Model-II.

Significantly, the curved surfaces shown in Figure 13 offered good guidance for the analysis of the wear behavior of the coating tested under different conditions. If the nanohardness of the wear track was relatively high, the roughness was low, and, the friction coefficient and wear rate of the coating were relatively low, then the wear form of coating was probably Model-I. The minor wear rate could be expected since the harder the coating, the more wear-resistant the compressed third body layer. Therefore, it could be proposed that the nanohardness value and the ratio of harder sublayers could be increased in the future design of TiAlSiN hardness-modulated multilayer coatings when the wear form is Model-I. On the contrary, the wear form is probably Model-II if the friction coefficient and wear rate of the coating are relatively high. Moreover, the lubrication of the coating should be carefully considered if the wear form is Model-II, since big-size abrasives result in a severe wear process.

Furtherly, the method could also be expected to be used in the optimization of TiAlSiN hardness-modulated multilayers with different modulation periods, as shown in the previous work. For example, a coating with more modulation periods has relatively smaller friction coefficients and wear rates, which tends to form a third body layer during the wear process [36]. The wear process of the coating is more likely to fall under Model-I, as illustrated in Figure 14a, and thus more hard sublayers can be added into the multilayer coating to achieve better wear resistance. In contrast, a coating with less modulation periods that

possesses relatively larger friction coefficients and wear rates should have more lubricated sublayers added to achieve better wear resistance.

5. Conclusions

TiAlSiN hardness-modulated multilayer coatings with regulable hardness and an adjustable amount of harder and softer sublayers could be prepared using the technique of PIIID. The well-bonded interfaces and the wear behavior under different normal loads and velocities were studied, and the following conclusions were drawn:

(1) The dense structure and the highly reinforced interfaces of the coating originated from ion bombardment and promoted the bonding, mechanical properties, and wear resistance of the coating to a large extent;
(2) A compressed and lubricated third body layer could be obtained under larger normal loads and resulted in a lower friction coefficient and wear rate, protecting the coating from being more severely worn, while the big-size and hardened abrasives accelerated the wear process under higher velocities;
(3) A full factorial analysis offered good guidance for wear form identification and the wear resistance optimization of TiAlSiN multilayer coating tested in the load–velocity coupling case;
(4) Hard sublayers should be added into multilayer coatings if the wear process conforms more to Model-I, which is probably needed in the conditions of larger normal load and smaller velocity, like sliding bearings. In contrast, more lubricated sublayers should be added, like in the case of high-speed cutting tools.

Supplementary Materials: The following supporting information can be downloaded at https://www.mdpi.com/article/10.3390/coatings14070821/s1: Table S1: ANOVA results for measured responses.

Author Contributions: Conceptualization, H.Q.; Software, Z.Z.; Validation, Z.L.; Formal analysis, J.Y. and H.Q.; Investigation, Z.Z.; Data curation, F.Z.; Writing—original draft, F.Z. and Z.Z.; Writing—review & editing, F.Z.; Visualization, Z.L.; Supervision, J.Y.; Funding acquisition, F.Z. All authors have read and agreed to the published version of the manuscript.

Funding: The authors are grateful for the financial support of the National Natural Science Foundation of China (No. 52305218), and the Natural Science Foundation of Sichuan Province (2023NSFSC0873).

Institutional Review Board Statement: Not applicable.

Informed Consent Statement: Not applicable.

Data Availability Statement: Data are contained within the article and Supplementary Materials.

Conflicts of Interest: The authors declare no conflict of interest.

References

1. Klaasen, H.; Kübarsepp, J. Wear of advanced cemented carbides for metalforming tool materials. *Wear* **2004**, *256*, 846–853. [CrossRef]
2. Pirso, J.; Letunovitš, S.; Viljus, M. Friction and wear behaviour of cemented carbides. *Wear* **2004**, *257*, 257–265. [CrossRef]
3. Roebuck, B.; Almond, E.A. Deformation and fracture processes and the physical metallurgy of WC–Co hardmetals. *Int. Mater. Rev.* **2013**, *33*, 90–112. [CrossRef]
4. Gagg, C.R.; Lewis, P.R. Wear as a product failure mechanism—Overview and case studies. *Eng. Fail. Anal.* **2007**, *14*, 1618–1640. [CrossRef]
5. Santecchia, E.; Hamouda, A.M.S.; Musharavati, F.; Zalnezhad, E.; Cabibbo, M.; Spigarelli, S. Wear resistance investigation of titanium nitride-based coatings. *Ceram. Int.* **2015**, *41*, 10349–10379. [CrossRef]
6. Ou, Y.X.; Wang, H.Q.; Ouyang, X.; Zhao, Y.Y.; Zhou, Q.; Luo, C.W.; Hua, Q.S.; Ouyang, X.P.; Zhang, S. Recent advances and strategies for high-performance coatings. *Prog. Mater. Sci.* **2023**, *136*, 101125. [CrossRef]
7. Sproul, W.D. New Routes in the Preparation of Mechanically Hard Films. *Science* **1996**, *273*, 889–892. [CrossRef] [PubMed]
8. Ma, G.; Wang, L.; Gao, H.; Zhang, J.; Reddyhoff, T. The friction coefficient evolution of a TiN coated contact during sliding wear. *Appl. Surf. Sci.* **2015**, *345*, 109–115. [CrossRef]

9. Łępicka, M.; Grądzka Dahlke, M.; Pieniak, D.; Pasierbiewicz, K.; Kryńska, K.; Niewczas, A. Tribological performance of titanium nitride coatings: A comparative study on TiN-coated stainless steel and titanium alloy. *Wear* **2019**, *422–423*, 68–80. [CrossRef]
10. Zhao, J.; Liu, Z.; Wang, B.; Song, Q.; Ren, X.; Wan, Y. Effects of Al content in TiAlN coatings on tool wear and cutting temperature during dry machining IN718. *Tribol. Int.* **2022**, *171*, 107540. [CrossRef]
11. Antonov, M.; Afshari, H.; Baronins, J.; Adoberg, E.; Raadik, T.; Hussainova, I. The effect of temperature and sliding speed on friction and wear of Si_3N_4, Al_2O_3, and ZrO_2 balls tested against AlCrN PVD coating. *Tribol. Int.* **2018**, *118*, 500–514. [CrossRef]
12. Huang, B.; Zhou, Q.; An, Q.; Zhang, E.g.; Chen, Q.; Liang, D.d.; Du, H.m.; Li, Z.m. Tribological performance of the gradient composite TiAlSiN coating with various friction pairs. *Surf. Coat. Technol.* **2022**, *429*, 127945. [CrossRef]
13. Liew, W.Y.H.; Lim, H.P.; Melvin, G.J.H.; Dayou, J.; Jiang, Z.T. Thermal stability, mechanical properties, and tribological performance of TiAlXN coatings: Understanding the effects of alloying additions. *J. Mater. Res. Technol.* **2022**, *17*, 961–1012. [CrossRef]
14. Lim, H.P.; Jiang, Z.T.; Melvin, G.J.H.; Nayan, N.; Chee, F.P.; Soon, C.F.; Hassan, N.; Liew, W.Y.H. A systematic investigation of the tribological behaviour of oxides formed on AlSiTiN, CrAlTiN, and CrAlSiTiN coatings. *Wear* **2023**, *512–513*, 204552. [CrossRef]
15. Schulz, W.; Joukov, V.; Köhn, F.; Engelhart, W.; Schier, V.; Schubert, T.; Albrecht, J. The Behavior of TiAlN and TiAlCrSiN Films in Abrasive and Adhesive Tribological Contacts. *Coatings* **2023**, *13*, 1603. [CrossRef]
16. Wang, S.q.; Chen, K.h.; Chen, L.; Zhu, C.j.; Li, P.; Du, Y. Effect of Al and Si additions on microstructure and mechanical properties of TiN coatings. *J. Cent. South Univ.* **2011**, *18*, 310–313. [CrossRef]
17. Das, S.; Guha, S.; Ghadai, R.; Swain, B.P. A comparative analysis over different properties of TiN, TiAlN and TiAlSiN thin film coatings grown in nitrogen gas atmosphere. *Mater. Chem. Phys.* **2021**, *258*, 123866. [CrossRef]
18. Philippon, D.; Godinho, V.; Nagy, P.M.; Delplancke Ogletree, M.P.; Fernández, A. Endurance of TiAlSiN coatings: Effect of Si and bias on wear and adhesion. *Wear* **2011**, *270*, 541–549. [CrossRef]
19. Tillmann, W.; Dildrop, M. Influence of Si content on mechanical and tribological properties of TiAlSiN PVD coatings at elevated temperatures. *Surf. Coat. Technol.* **2017**, *321*, 448–454. [CrossRef]
20. Pei, F.; Liu, H.J.; Chen, L.; Xu, Y.X.; Du, Y. Improved properties of TiAlN coating by combined Si-addition and multilayer architecture. *J. Alloys Compd.* **2019**, *790*, 909–916. [CrossRef]
21. Ma, H.; Miao, Q.; Zhang, G.; Liang, W.; Wang, Y.; Sun, Z.; Lin, H. The influence of multilayer structure on mechanical behavior of TiN/TiAlSiN multilayer coating. *Ceram. Int.* **2021**, *47*, 12583–12591. [CrossRef]
22. Zhao, S.; Zhang, J.; Zhang, Z.; Wang, S.; Zhang, Z. Microstructure and mechanical properties of (Ti,Al,Zr)N/(Ti,Al,Zr,Cr)N films on cemented carbide substrates. *Int. J. Miner. Metall. Mater.* **2014**, *21*, 77–81. [CrossRef]
23. Cao, H.; Yang, J.; Luo, W.; Li, Y.; Qi, F.; Zhao, N.; Lu, L.; Ouyang, X. Influence of film structure on the microstructure and properties of TiAlN coatings on Al-Si alloys. *Mater. Charact.* **2022**, *189*, 111996. [CrossRef]
24. Sampath Kumar, T.; Balasivanandha Prabu, S.; Manivasagam, G.; Padmanabhan, K.A. Comparison of TiAlN, AlCrN, and AlCrN/TiAlN coatings for cutting-tool applications. *Int. J. Miner. Metall. Mater.* **2014**, *21*, 796–805. [CrossRef]
25. Cai, F.; Wang, J.; Zhou, Q.; Zhang, S.; Zheng, J.; Wang, Q.; Kim, K.H. Reduced delamination and improved cutting performance of TiAlSiN multilayer coated cutter by tailoring the adhesion layers and intermediate layers. *Wear* **2022**, *488–489*, 204135. [CrossRef]
26. Li, G.; Li, L.; Han, M.; Luo, S.; Jin, J.; Wang, L.; Gu, J.; Miao, H. The Performance of TiAlSiN Coated Cemented Carbide Tools Enhanced by Inserting Ti Interlayers. *Metals* **2019**, *9*, 918. [CrossRef]
27. Wei, Z.; Xu, X. FEM simulation on impact resistance of surface gradient and periodic layered bionic composites. *Compos. Struct.* **2020**, *247*, 112428. [CrossRef]
28. Kabir, M.S.; Zhou, Z.; Xie, Z.; Munroe, P. Scratch adhesion evaluation of diamond like carbon coatings with alternate hard and soft multilayers. *Wear* **2023**, *518–519*, 204647. [CrossRef]
29. Khadem, M.; Penkov, O.V.; Yang, H.K.; Kim, D.E. Tribology of multilayer coatings for wear reduction: A review. *Friction* **2017**, *5*, 248–262. [CrossRef]
30. Hassani, S.; Klemberg-Sapieha, J.E.; Bielawski, M.; Beres, W.; Martinu, L.; Balazinski, M. Design of hard coating architecture for the optimization of erosion resistance. *Wear* **2008**, *265*, 879–887. [CrossRef]
31. Kolchev, S.; Kolaklieva, L.; Chitanov, V.; Cholakova, T.; Zlatareva, E.; Kovacheva, D.; Atanasova, G.; Kakanakov, R. The Role of Period Modulation on the Structure, Composition and Mechanical Properties of Nanocomposite Multilayer TiAlSiN/AlSiN Coatings. *Coatings* **2023**, *13*, 1546. [CrossRef]
32. He, N.; Li, H.; Ji, L.; Liu, X.; Zhou, H.; Chen, J. High temperature tribological properties of TiAlSiN coatings produced by hybrid PVD technology. *Tribol. Int.* **2016**, *98*, 133–143. [CrossRef]
33. Yue, Q.B.; He, H.B.; Li, H.Y.; Zhang, J.; Li, Y.M.; Ma, L. Research on Friction Characteristics of AlCrN and TiAlSiN Coatings and Properties of Coated Tools. *Int. J. Precis. Eng. Manuf.* **2019**, *20*, 1581–1589. [CrossRef]
34. Mourlas, A.; Psyllaki, P.; Chaliampalias, D.; Vourlias, G.; Kolaklieva, L.; Kakanakov, R. Tribological Behaviour of Gradient TiAlSiN Superhard Coatings. *Key Eng. Mater.* **2016**, *674*, 207–212. [CrossRef]
35. Zhao, F.; Wang, L.; Wang, X. Microstructure and properties of TiAlSiN ultra-hard coatings prepared by plasma immersion ion implantation and deposition with TiAlSi alloy cathodes. *Vacuum* **2020**, *174*, 109194. [CrossRef]
36. Zhao, F.; Ge, Y.; Wang, L.; Wang, X. Tribological and mechanical properties of hardness-modulated TiAlSiN multilayer coatings fabricated by plasma immersion ion implantation and deposition. *Surf. Coat. Technol.* **2020**, *402*, 126475. [CrossRef]

37. Yu, D.; Wang, C.; Cheng, X.; Zhang, F. Microstructure and properties of TiAlSiN coatings prepared by hybrid PVD technology. *Thin Solid Film.* **2009**, *517*, 4950–4955. [CrossRef]
38. Zhirkov, I.; Petruhins, A.; Polcik, P.; Kolozsvári, S.; Rosen, J. Generation of super-size macroparticles in a direct current vacuum arc discharge from a Mo-Cu cathode. *Appl. Phys. Lett.* **2016**, *108*, 054103. [CrossRef]
39. Carvalho, N.J.M.; Zoestbergen, E.; Kooi, B.J.; De Hosson, J.T.M. Stress analysis and microstructure of PVD monolayer TiN and multilayer TiN/(Ti,Al)N coatings. *Thin Solid Film.* **2003**, *429*, 179–189. [CrossRef]
40. Wang, L.; Zhao, S.; Xie, Z.; Huang, L.; Wang, X. MoS_2/Ti multilayer deposited on 2Cr13 substrate by PIIID. *Nucl. Instrum. Methods Phys. Res. Sect. B* **2008**, *266*, 730–733. [CrossRef]
41. Xie, Z.W.; Wang, L.P.; Wang, X.F.; Huang, L.; Lu, Y.; Yan, J.C. Influence of high temperature annealing on the structure, hardness and tribological properties of diamond-like carbon and TiAlSiCN nanocomposite coatings. *Appl. Surf. Sci.* **2011**, *258*, 1206–1211. [CrossRef]
42. Wang, Z.; Li, X.; Wang, X.; Cai, S.; Ke, P.; Wang, A. Hard yet tough V-Al-C-N nanocomposite coatings: Microstructure, mechanical and tribological properties. *Surf. Coat. Technol.* **2016**, *304*, 553–559. [CrossRef]
43. Liu, C.; Sun, J. Effect of load on friction and wear behaviors of alumina matrix ceramic guideway materials. *J. Alloys Compd.* **2018**, *743*, 268–273. [CrossRef]
44. Zhu, Y.; Dong, M.; Li, J.; Wang, L. Wear failure mechanism of TiSiN coating at elevated temperatures. *Appl. Surf. Sci.* **2019**, *487*, 349–355. [CrossRef]
45. Shum, P.W.; Xu, Y.F.; Zhou, Z.F.; Cheng, W.L.; Li, K.Y. Study of TiAlSiN coatings post-treated with N and C+N ion implantations. Part 2: The tribological analysis. *Wear* **2012**, *274–275*, 274–280. [CrossRef]
46. Al Rjoub, A.; Cavaleiro, A.; Yaqub, T.B.; Evaristo, M.; Figueiredo, N.M.; Fernandes, F. TiAlSiN(Ag) coatings for high temperature applications: The influence of Ag alloying on the morphology, structure, thermal stability and oxidation resistance. *Surf. Coat. Technol.* **2022**, *442*, 128087. [CrossRef]
47. Hardcastle, F.D.; Wachs, I.E. Raman spectroscopy of chromium oxide supported on Al_2O_3, TiO_2 and SiO_2: A comparative study. *J. Mol. Catal.* **1988**, *46*, 173–186. [CrossRef]
48. Andrade, C. The P Value and Statistical Significance: Misunderstandings, Explanations, Challenges, and Alternatives. *Indian J. Psychol. Med.* **2019**, *41*, 210–215. [CrossRef]
49. Voevodin, A.A.; Zabinski, J.S. Supertough wear-resistant coatings with 'chameleon' surface adaptation. *Thin Solid Film.* **2000**, *370*, 223–231. [CrossRef]
50. Lü, W.; Li, G.; Zhou, Y.; Liu, S.; Wang, K.; Wang, Q. Effect of high hardness and adhesion of gradient TiAlSiN coating on cutting performance of titanium alloy. *J. Alloys Compd.* **2020**, *820*, 153137. [CrossRef]
51. Cao, X.; He, W.; Liao, B.; Zhou, H.; Zhang, H.; Tan, C.; Yang, Z. Sand particle erosion resistance of the multilayer gradient TiN/Ti coatings on Ti6Al4V alloy. *Surf. Coat. Technol.* **2019**, *365*, 214–221. [CrossRef]
52. Gnyusov, S.F.; Fedin, E.A.; Tarasov, S.Y. The effect of counterbody on tribological adaptation of an electron beam deposited HSS M2 steel coating in a range of sliding speeds and normal loads. *Tribol. Int.* **2021**, *161*, 107109. [CrossRef]
53. Deng, F.; Tsekenis, G.; Rubinstein, S.M. Simple Law for Third-Body Friction. *Phys. Rev. Lett.* **2019**, *122*, 135503. [CrossRef] [PubMed]
54. Niu, Z.; Zhou, W.; Wang, C.; Cao, Z.; Yang, Q.; Fu, X. Fretting wear mechanism of plasma-sprayed CuNiIn coating on Ti-6Al-4V substrate under plane/plane contact. *Surf. Coat. Technol.* **2021**, *408*, 126794. [CrossRef]